Check for updates

An Investigation of Titanium/Silicon Oxide-CNTs Anode Material for Lithium-Ion Batteries

Wenshan Zhang,[a] Wensheng Li,[a] and Xiaoping Zhou*[a]

Discovering a high-performance (high rate capability, high specific capacity, and good stability) anode material for automobile battery applications is a great challenge. A titanium/silicon oxide-CNTs ($Ti_mSi_nO_l$-CNTs) is synthesized and tested as anode material for lithium-ion batteries. High specific capacity (278 $mAhg^{-1}$ at 100 $mA\,g^{-1}$), high rate capability (156 $mAh\,g^{-1}$ at 4000 $mA\,g^{-1}$), and good stability (maintains 278 $mAhg^{-1}$ after 200 cycles) are reached over $Ti_mSi_nO_l$-CNTs. The as-synthesized $Ti_mSi_nO_l$-CNTs has a particle structure that $Ti_mSi_nO_l$ encapsulates CNTs with CNTs ends stretching out of the particles. In the $Ti_mSi_nO_l$ phase, the TiO_2 crystal seeds are formed and encapsulated in amorphous SiO_y boundaries, which have sub-nano pores. The high performance properties of $Ti_mSi_nO_l$-CNTs could come from the synergetic combination of (1) the excellent electronic conductivity of CNTs and the amorphous carbon in $Ti_mSi_nO_l$-CNTs, (2) the high Li^+ intaking capability of the TiO_2 crystal seeds, (3) the high electrochemical activity of SiO_y, (4) the high Li^+ insertion/extraction kinetics in the small TiO_2 crystal seeds and the amorphous SiO_y with sub-nano pores, and (5) the high volume change tolerance offered by the CNTs binder and the amorphous SiO_y.

1. Introduction

In the investigations of anode materials for lithium-ion batteries (LIBs), three types of materials are reported. They are the intercalation type materials (e.g., graphite or lithium titanate),[1–4] metal and alloy materials (e.g., lithium, tin, tin selenide, or silicon),[5–8] and reduction/oxidation type materials (e.g., WO_3 and ReS_2).[9–11]

Graphite is widely employed as the anode material due to its high specific capacity, easy availability, non-toxic, and cheap price. However, the low lithium ion diffusion rate[1] of graphite limits it's applications as anode material in high rate requiring batteries for electric vehicles. The commercialized $Li_4Ti_5O_{12}$ has many priorities, such as high rate capability, high safety, and long cycling life-time.[3–4] However, comparing with graphite, the low specific capacity of $Li_4Ti_5O_{12}$ (theoretical capacity 175 $mAhg^{-1}$) limits it's applications in personal vehicles that have limited volume. Silicon and tin have been developed recently with higher theoretical specific capacities of 4200 $mAhg^{-1}$ and 990 $mAhg^{-1}$, respectively. However, they suffer from large volume expansion/contraction, which is detrimental for cycling stability.[8,12]

A number of metal oxides have been widely investigated as LIB anodes. However, these materials have very poor cyclability due to the volume change during lithiation/de-lithiation processes, low electronic conductivity, unstable solid electrolyte interface layer, and high irreversible capacity due to the formation of Li_2O.[13]

[a] W. Zhang, W. Li, Prof. X. Zhou
Department of Chemical Engineering
Hunan University
Changsha, Hunan 410082, P. R. China
E-mail: hgx2002@hnu.edu.cn

Supporting information for this article is available on the WWW under https://doi.org/10.1002/batt.201900178

The TiO_2 as a potential anode material for lithium ion batteries has many advantages, such as abundant, non-toxic, low-cost, environmentally benign natures,[14] good lithium ion conductivity,[15] and an increase in electrical conductivity of the lithiated TiO_2 (Li_xTiO_2, $0 \leq x \leq 1$) during lithiation process.[16–18] TiO_2 or promoted TiO_2 is widely investigated as an anode material for lithium ion batteries.[13,19–21] Among the polymorphs of TiO_2, rutile TiO_2 can only accommodate negligible Li^+ ions (<0.1 Li per TiO_2 unit) at room temperature.[15,22] However, the anatase TiO_2 shows fast Li^+ insertion/extraction along (001) plane of TiO_2.[16,17] In comparison with the rutile structure, the uptake of Li^+ appears more facile in the anatase lattice. It has a tetragonal body-centered space group $I4_1/amd$, and is comprised of TiO_6 octahedra sharing two adjacent edges with two other octahedra, so that planar double chains are formed.[23] The diffusion of Li^+ ions in an anatase framework occurs along a reaction path connecting the octahedral interstitial sites.[24–26] The anatase TiO_2 has a theoretical capacity of 335 mAg^{-1} (calculated as $LiTiO_2$).[13,19–21] However, practically, the theoretical capacity has rarely been reached. The reason is that the further Li-ion insertion in TiO_2 is blocked because of the strong repulsive force between Li ions as the insertion ratio is greater than 0.5 (167.5 $mAhg^{-1}$, as $x = 0.5$ in Li_xTiO_2),[27,28] which greatly limits the applications of TiO_2 as anode material. The other drawback of TiO_2 is the poor conductivity of lithium ions and electrons in the bulk of TiO_2, limiting the electrochemical performance of TiO_2.

In order to improve the charge and Li^+ ion transport properties, TiO_2 has been fabricated into varieties of nanostructures. The fabrication of TiO_2 into nanostructures reduces the diffusion length of Li-ion insertion/extraction and improves the electrical conductivity of the electrode materials. Gao et al.[29] synthesized anatase nanotubes and reached first discharge and charge capacities of 340 and 200 $mAhg^{-1}$, respectively. Similar results were also obtained by Li et al.[30]

© 2020 Wiley-VCH Verlag GmbH & Co. KGaA, Weinheim

and Zhang et al.[31] Bao et al.[14] reported nano-porous anatase nano-rods, in which the nano-porous structure demonstrated a good cyclability and a high rate capability. Kim and Cho[32] reported both anatase TiO_2 nanotubes and nano-rods and they found that this type of materials has high rate capability. Nano-rods prepared by Kim and Cho gave specific capacities of 200 and 160 $mAhg^{-1}$ at 0.5 and 10 *C* rates, respectively.

In searching for high performance TiO_2 containing anode materials, TiO_2 containing multi-component composites are investigated. Layer material (The MoS_2 layers are synthesized over TiO_2 sheets and TiO_2 sheets are synthesized over graphene oxide) was synthesized and tested as anode material for lithium cells by Zhao et al.[33] High specific capacity, excellent stability, and high rate capability (802 $mAh\,g^{-1}$ at 100 mAg^{-1} and 511 $mAhg^{-1}$ at 2000 mAg^{-1}) are obtained. However, strong corrosive chemicals HCl/H_2O, $TiCl_4$, and HF/H_2O are used in the synthesis process of the material. It could be difficult in practical scale up production of the material. Wang and co-workers reported a TiO_2 coated Ge-graphene Nanofiber,[34] which has excellent specific capacity (1050 $mAhg^{-1}$ at 1000 mAg^{-1}). However, the material fails to deliver the necessary stability and it's containing of large amount of expensive Ge is also the fatal drawback, which hinder it's practical applications. Apart from the above mentioned TiO_2 containing anode materials, there are materials containing TiO_2 and other metal oxides, such as TiO_2 coated ZnO nanorods[35,36] and TiO_2 nanotubes filled with SnO_2[37] nanocrystals, which are synthesized and tested as anode materials for lithium ion batteries. However, these materials are not stable in discharge/charge cycles.

Fong et al.[38] prepared TiO_2-SiO_2 composite felt (containing 75 wt.% of anatase TiO_2 nanofibers and 25 wt.% of amorphous SiO_2 nanofibers) by the dual-spinneret electrospinning technique followed by heat treatment at 500 °C.This is a mechanical mixing of TiO_2 nanofibers with SiO_2 nanofibers. The desired high specific capacity and high stability are not reached. Zhao et al. prepared and tested a TiO_2 doped SiO_x (SiO_x as the major component) anode material.[39] The authors declare that the doping of TiO_2 nanoparticles in SiO_x particles could effectively enhances the electronic and lithium ionic conductivities of the SiO_x particles and releases the structure stress caused by alloying/dealloying of Si component. The synergetic combination of these advantages enables the material to have excellent electrochemical performances (a stable specific capacity of about 910 $mAh\,g^{-1}$ is achieved after 200 cycles at 100 mAg^{-1}). However, the material losses more than half of its specific capacity within the first 30 cycles of discharging/charging.

In materials containing TiO_2 as the major component are farther promoted by introducing electronic conductive carbon materials. Cao et al.[40] prepared and tested a TiO_2 coated carbon nanotubes and reached a specific capacity of 238 $mAhg^{-1}$ at 5000 mAg^{-1} (without CNTs, the specific capacity of TiO_2 is only 62 $mAhg^{-1}$ at 5000 mAg^{-1}). The CNTs offer sufficient electrons for TiO_2 nanoshell to store the Li ions, and TiO_2 nanoshell provides Li ions to CNTs to store electrons. Comparing with CNTs, the organic compound derived carbon could extend to almost all the surface of TiO_2 crystals and construct an even well electronic conductive network for TiO_2 nanocrystals. Carbon doped TiO_2 nanotubes have been reported by Xu et al.[41] A specific capacity of 291.7 $mAhg^{-1}$ is reached at the current density of 70 mAg^{-1}. After 30 cycles, the reversible capacity still remains 211 $mAhg^{-1}$. Although high weight based specific capacities are reached over TiO_2 coated CNTs or carbon doped TiO_2 nanotubes, the volume based specific capacities of the materials are very low, and also, these materials usually have very big specific surface areas, which leads to electrode processing difficulties. Although by integrating electronic conductive carbon into TiO_2 phase could reach relatively high specific capacities, the performance of TiO_2 based materials is still waiting for farther promotion in terms of the specific capacity, cycling stability, and high rate capability.

To the best of our knowledge, the investigations dedicated to the foreign element doped TiO_2 anode materials (the foreign element is doped into the bulk of TiO_2 phase) for lithium ion batteries are rare. Here we report a new preparation method for the synthesis of a titanium oxide based material, intending to promoting the electrochemical performances. In the topic preparation method, the polymer ($Ti_mSi_n(OCH_2CH_2O)_{2(m+n)}$-CNTs) is prepared from ethylene glycol, titanium tetra-alkoxide, and silicon tetra-alkoxide in the presence of CNTs and an amine catalyst. After calcination in nitrogen, the compounds decompose to $Ti_mSi_nO_l$-CNTs and amorphous carbon (amorphous carbon is formed from the decomposition of diols). In this material, the amorphous carbon and the CNTs are supposed to form an excellent electronic conductive network in the material. The amorphous carbon could enhance the electronic conductivity inside the particles, while the CNTs conductive framework could enhance the electron transport both inside the particles and among nearby particles. Introducing SiO_y into TiO_x-CNTs material is intending to improve the structure stability and raise the specific capacity of the material.

2. Results and Discussion

The synthesis process of $Ti_mSi_nO_l$-CNTs is given in Scheme 1. The tetrapropyl orthosilicate and titanium (IV) tetraisopropoxide are allowed to react with anhydrous ethylene glycol by employing *N*,*N*-dimethylhexadecylamine as catalyst in the presence of CNTs to obtain a solid material. The solid material is supposed to be a titanium-silicon ethylene glycol polymer $Ti_mSi_n(OCH_2CH_2O)_{2(m+n)}$ with CNTs. In the resulted solid polymer, the CNTs are encapsulated inside the polymer to yield $Ti_mSi_n(OCH_2CH_2O)_{2(m+n)}$-CNTs. After calcination in nitrogen, $Ti_mSi_n(OCH_2CH_2O)_{2(m+n)}$-CNTs decomposes to $Ti_mSi_nO_l$-CNTs, which has CNTs encapsulated in titanium-silicon oxides ($Ti_mSi_nO_l$-CNTs).

The TGA analysis shows that $Ti_mSi_n(OCH_2CH_2O)_{2(m+n)}$-CNTs has two weight loss temperature regions between 25 and 800 °C (Figure 1). The first weight loss happens between 25 and 188 °C, which could be attributed to the desorption of alcohols (propanol, isopropanol, ethanol, and ethylene glycol). The second weight loss happens between 188 and 360 °C, which could be because of the decomposition of the polymer $Ti_mSi_n(OCH_2CH_2O)_{2(m+n)}$-CNTs to yield $Ti_mSi_nO_l$-CNTs. The decomposi-

© 2020 Wiley-VCH Verlag GmbH & Co. KGaA, Weinheim

25666223, 2020, 5, Downloaded from https://chemistry-europe.onlinelibrary.wiley.com/doi/10.1002/batt.201900178 by University of Ulsan, Wiley Online Library on [11/11/2025]. See the Terms and Conditions (https://onlinelibrary.wiley.com/terms-and-conditions) on Wiley Online Library for rules of use; OA articles are governed by the applicable Creative Commons License

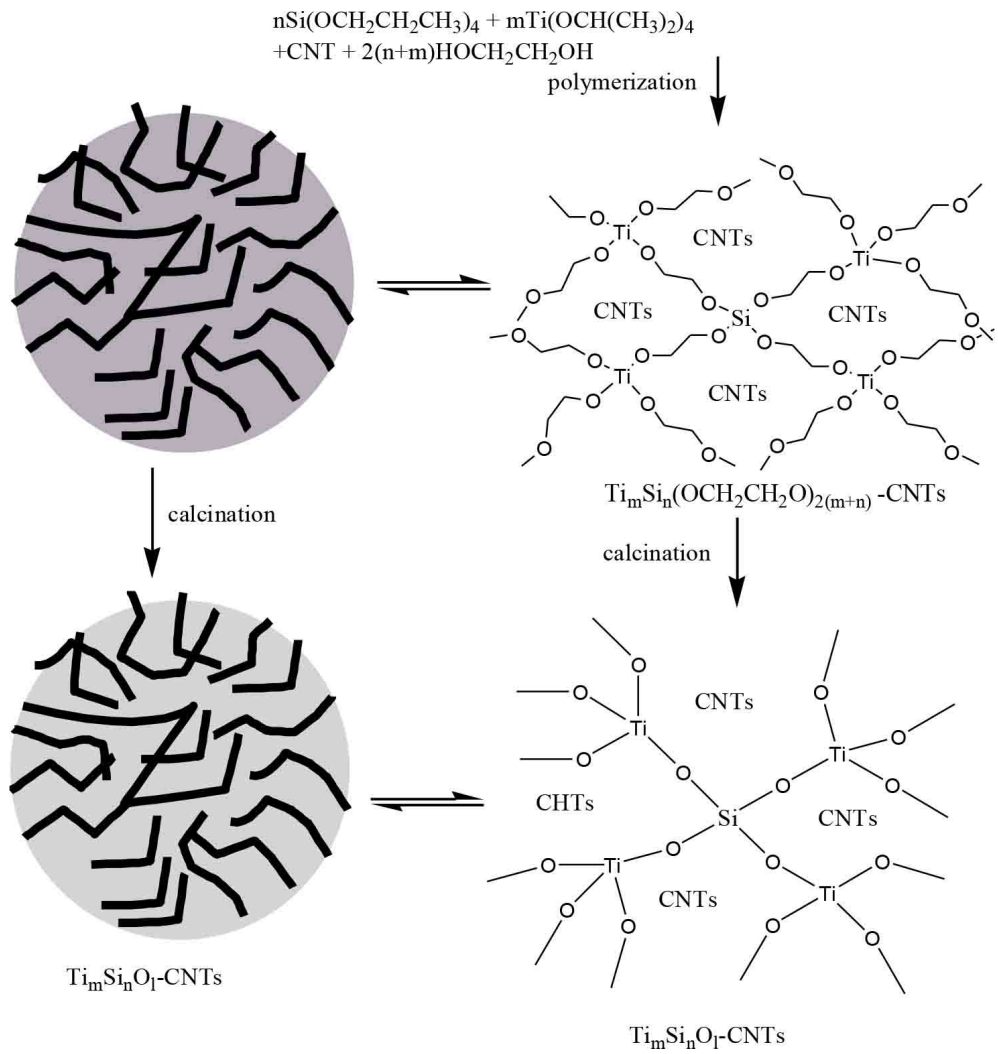

Scheme 1. Material synthesis.

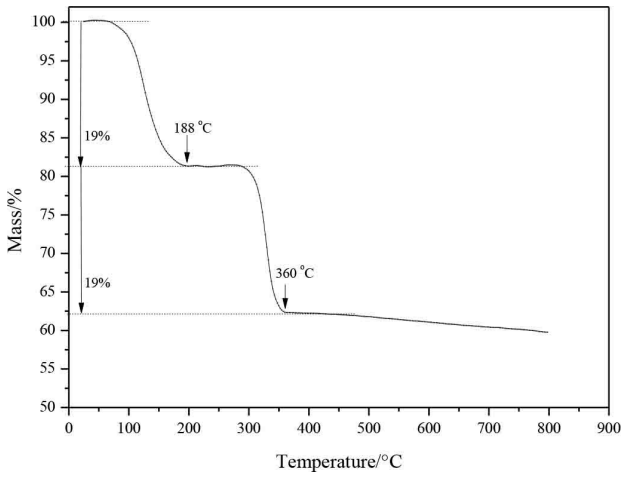

Figure 1. The TG analysis of $Ti_mSi_n(OCH_2CH_2O)_{2(m+n)}$-CNTs.

tion of $Ti_mSi_n(OCH_2CH_2O)_{2(m+n)}$-CNTs has almost been completed at 360 °C. The final material $Ti_mSi_nO_l$-CNTs (calcined at 400 °C) contains 74.56 wt% of TiO_2, 6.22 wt% of SiO_2, and 18.61 wt% of carbon (obtained from the XRF analysis).

The specific surface areas of $Ti_mSi_nO_l$-CNTs calcined at different temperatures are given in Table S1. The specific surface area changes very little (39.1–36.4 m^2/g) from 300 to 400 °C. The TGA results show that from 300 to 400 °C, the major reaction could be the decomposition of polymer $Ti_mSi_n(OCH_2CH_2O)_{2(m+n)}$-CNTs to yield a solid $Ti_mSi_nO_l$-CNTs. When $Ti_mSi_nO_l$-CNTs is prepared from 400 to 700 °C, the specific surface area of $Ti_mSi_nO_l$-CNTs increases from 36.4 to 65.8 m^2/g. The possible reason could be that the crystallization process of amorphous TiO_2 leads to the formation of cracks and pores in the $Ti_mSi_nO_l$-CNTs particles. This will be addressed in the XRD and SEM characterization sections. In viewpoint of practical applications, electrode materials having smaller specific surface areas favor the electrode processing process. Hence, the material calcined at 400 °C is preferred. The TiO_x-CNTs calcined at 400 °C has bigger specific surface area (97.3 m^2/g) than $Ti_mSi_nO_l$-CNTs that is calcined at temperatures from 300 to 700 °C.

© 2020 Wiley-VCH Verlag GmbH & Co. KGaA, Weinheim

25666223, 2020, 5, Downloaded from https://chemistry-europe.onlinelibrary.wiley.com/doi/10.1002/batt.201900178 by University of Ulsan, Wiley Online Library on [11/11/2025]. See the Terms and Conditions (https://onlinelibrary.wiley.com/terms-and-conditions) on Wiley Online Library for rules of use; OA articles are governed by the applicable Creative Commons License

The XRD patterns of $Ti_mSi_nO_l$-CNTs and TiO_x-CNTs calcined at various temperatures are given in Figure 2. When the material is calcined below 400 °C, the resulted $Ti_mSi_nO_l$-CNTs is amorphous. When the material is calcined above 500 °C, the XRD pattern shows the pattern of anatase TiO_2 (according to JPCD card NO. 21-1272.). At even high calcination temperatures, from 500 to 700 °C, the peaks of anatase TiO_2 become even sharper and stronger, which indicates that the anatase crystals become more well crystalized (Figure 2a). However, the XRD pattern of TiO_x-CNTs in Figure 2b shows the formation of anatase TiO_2 at 400 °C. The diffraction peaks of anatase become very strong at 500 °C. From 500 to 600 °C, the anatase TiO_2 phase in TiO_x-CNTs is being converted to rutile TiO_2. At 600 °C, the peaks of both anatase and rutile are very weak, indicating that anatase phase is transforming to rutile phase at 600 °C. This result is consistent with the literature report.[42] The anatase phase is fully converted to rutile phase at 700 °C in TiO_x-CNTs. The results show that the presence of SiO_2 (even only 6.22 wt %) in $Ti_mSi_nO_l$-CNTs could hinder the crystallization of TiO_2 at higher temperature. The estimated crystal sizes of TiO_2 in $Ti_mSi_nO_l$-CNTs and TiO_x-CNTs calcined at 500 °C are 10.9 and 19.6 nm, respectively (Table S2). When $Ti_mSi_nO_l$-CNTs and TiO_x-CNTs are obtained from the same calcination temperatures between 500 to 700 °C, the crystal size of TiO_2 in $Ti_mSi_nO_l$-CNTs is smaller than that of TiO_2 in TiO_x-CNTs (Table s2). The other effect of introducing SiO_2 into TiO_x-CNTs could stabilize TiO_2 in anatase phase up to 700 °C, without being converted to rutile structure. In reported literature, SiO_2 has been used to help stabilizing the anatase TiO_2 up to high calcination temperature.[42] Anatase phase favors Li^+ ion intercalation/deintercalation.[15,22]

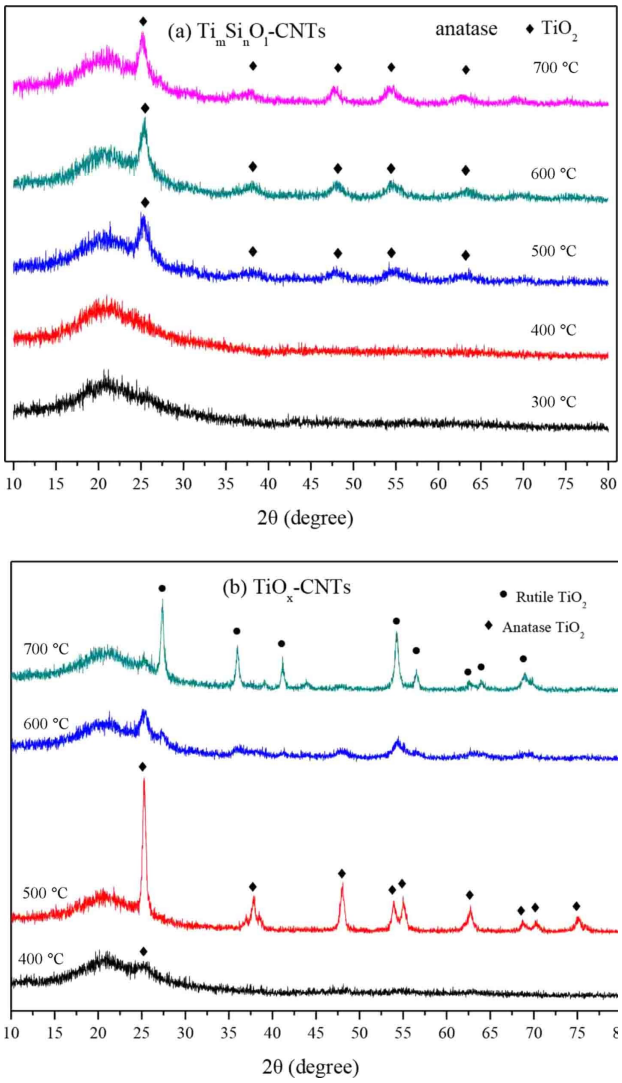

Figure 2. The XRD patterns of (a) $Ti_mSi_nO_l$-CNTs and (b) TiO_x-CNTs calcined at different temperatures.

The XRD and specific surface area characterizations of the $Ti_mSi_nO_l$-CNTs calcined at different temperatures show that, with the increase of the calcination temperature from 400 to 700 °C, there are more and more nearby Ti^{4+} ions moving out from the solid solution phase $Ti_mSi_nO_l$ to form the anatase crystals. The moving out of Ti^{4+} ions from the solid solution phase $Ti_mSi_nO_l$ might also generate tensions in the solid solution phase and create cracks and pores around these TiO_2 crystals. This could be the reason that leads to the relatively higher specific surface area of the material that is calcined at relatively higher temperatures.

The SEM images of $Ti_mSi_n(OCH_2CH_2O)_{2(m+n)}$-CNTs and $Ti_mSi_nO_l$-CNTs (calcined at 400 °C) are given in Figure 3ab. The image of $Ti_mSi_n(OCH_2CH_2O)_{2(m+n)}$-CNTs (Figure 3a) shows that the CNTs are encapsulated in the bulk of the polymer $Ti_mSi_n(OCH_2CH_2O)_{2(m+n)}$ with some CNTs ends stretching out of the particles (marches our original design as shown in Scheme 1). After calcination at 400 °C (Figure 3b), $Ti_mSi_nO_l$-CNTs is obtained. The resulted $Ti_mSi_nO_l$-CNTs is an amorphous material (the XRD in Figure 2). Again, on the particles of $Ti_mSi_nO_l$-CNTs, there are CNT ends stretching out of the surface. These CNT ends belong to different particles could easily get in touching with each other, which favors electron transfer among the nearby particles. Also, these encapsulated CNTs could enforce the strength of the particles to tolerate the volume change, while in charge/discharge process. The results are consistent with our original idea for the material synthesis. On comparing the sample calcined at 400 °C with that calcined at 600 °C (Figure S1a), the $Ti_mSi_nO_l$ phase in $Ti_mSi_nO_l$-CNTs calcined at 600 °C becomes porous (Figure S1b). The SEM characterization results are consistent with that of the specific surface measurements and XRD characterizations.

In Figure 3cd, the TEM image and diffraction pattern show that even $Ti_mSi_n(OCH_2CH_2O)_{2(m+n)}$-CNTs was calcined at relatively lower temperature (400 °C), anatase crystal seeds are formed. The lattice planes (101) and (001) of anatase TiO_2 are identified.[43,44] The TEM image of Fig S2 shows that the anatase TiO_2 seeds (with average size of about 5 nm) are actually formed at 400 °C. Around the anatase crystal seeds, there are boundaries, where sub-nano pores (below 0.3 nm) can be observed. These pores are potentially ideal Li ion diffusion channels. The boundaries should mainly contain amorphous SiO_y (since that the Ti^{4+} ions have migrated out to form the anatase seeds). The TEM characterization results are consistent

© 2020 Wiley-VCH Verlag GmbH & Co. KGaA, Weinheim

25666223, 2020, 5, Downloaded from https://chemistry-europe.onlinelibrary.wiley.com/doi/10.1002/batt.201900178 by University of Ulsan, Wiley Online Library on [11/11/2025]. See the Terms and Conditions (https://onlinelibrary.wiley.com/terms-and-conditions) on Wiley Online Library for rules of use; OA articles are governed by the applicable Creative Commons License

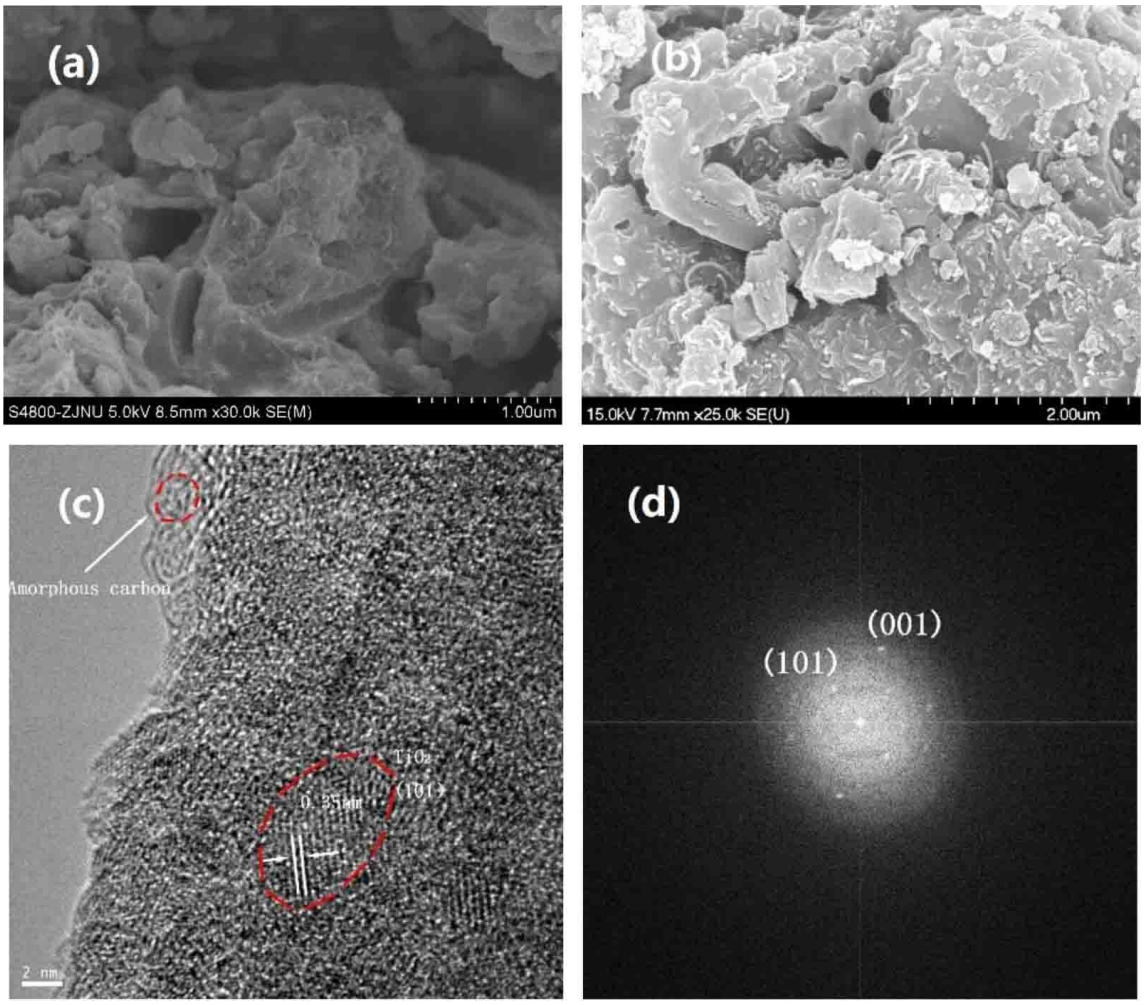

Figure 3. The SEM images of (a) $Ti_mSi_n(OCH_2CH_2O)_{2(m+n)}$-CNTs and (b) $Ti_mSi_nO_l$-CNTs calcined at 400 °C. (c) The TEM image of $Ti_mSi_nO_l$-CNTs calcined at 400 °C, and (d) the diffraction pattern of $Ti_mSi_nO_l$-CNTs calcined at 400 °C.

with that of the specific surface measurements, XRD characterizations, and the SEM characterizations.

Figure 4a gives the XPS of Si 2p of fresh $Ti_mSi_nO_l$-CNTs. The results show that the Si exists in Si^{4+} (103.3 eV), Si^{3+}(102.7 eV), Si^{2+}(101.4 eV), and Si^{+} (100.2 eV) valence states,[45–46] which have XPS peak area percentages of 18.3, 67.0, 11.4, and 3.3 %, respectively. The results indicate that the Si^{4+} ions are reduced and the majority of silicon atoms are in lower valence states (below 4+). The Si^{3+} is the major species. Figure 4b gives the XPS of Si 2p from $Ti_mSi_nO_l$-CNTs electrode (versus metal Li electrode) after the cell was charge/discharged 20 cycles and finally charged to 2.60 V versus metal lithium. The peaks of Si 2p are at 104.5 eV for Si^{4+}, 102.5 eV for Si^{3+}, 101.5 eV for Si^{2+}, and 99.9 eV for Si^{+}. After experienced 20 cycles of charge/discharge, the valence states of silicon shift to even low side. In this case, the Si^{2+} becomes the major species (standing for 62.70 % of peak area). The results indicate that the irreversibility of the material in the first cycle mainly comes from the SiO_y phase. The lower Si valence in SiO_y corresponds to a lower y value and therefore a higher electrochemical activity of SiO_y.[39] The XPS characterizations indicate that the silicon species are involved in the electrochemical reactions.

The XPS of Ti $2p_{3/2}$ and $2p_{1/2}$ are given in Figure 4c**d**. In the fresh $Ti_mSi_nO_l$-CNTs (Figure 4c), the broad Ti $2p_{3/2}$ and $2p_{1/2}$ peaks can be divided into peaks of Ti^{4+} and Ti^{3+} species, respectively (456.9 and 455.9 eV for Ti $2p_{3/2}$, 464.6 and 463.8 eV for $2p_{1/2}$).[47,48] The major part of Ti atoms are in Ti^{4+} valence state. The Ti^{3+} valence state ions stand for about 28.2 % of peak area of Ti $2p_{3/2}$ and $2p_{1/2}$, indicating that the carbothermal reduction occurs between Ti^{4+} and C. Such mixed valence states of Ti are beneficial for electron transportation in $Ti_mSi_nO_l$-CNTs particles. After the cell was charge/discharged for 20 cycles and finally charged to 2.60 V versus metal lithium (Figure 4d), the peak area percentage of Ti^{3+} species changes to 31.1 %. The results also show that the peaks of Ti $2p_{3/2}$ and $2p_{1/2}$ shift towards lower bonding energy direction, indicating that the whole system is in a more reduced states, which render the material more electronic conductive.

The XPS characterization shows that there is large amount of Ti^{4+} ions and Si^{4+} ions reduced to lower valence states in the fresh $Ti_mSi_nO_l$-CNTs. The partially reduced titanium oxide

© 2020 Wiley-VCH Verlag GmbH & Co. KGaA, Weinheim

25666223, 2020, 5, Downloaded from https://chemistry-europe.onlinelibrary.wiley.com/doi/10.1002/batt.201900178 by University of Ulsan, Wiley Online Library on [11/11/2025]. See the Terms and Conditions (https://onlinelibrary.wiley.com/terms-and-conditions) on Wiley Online Library for rules of use; OA articles are governed by the applicable Creative Commons License

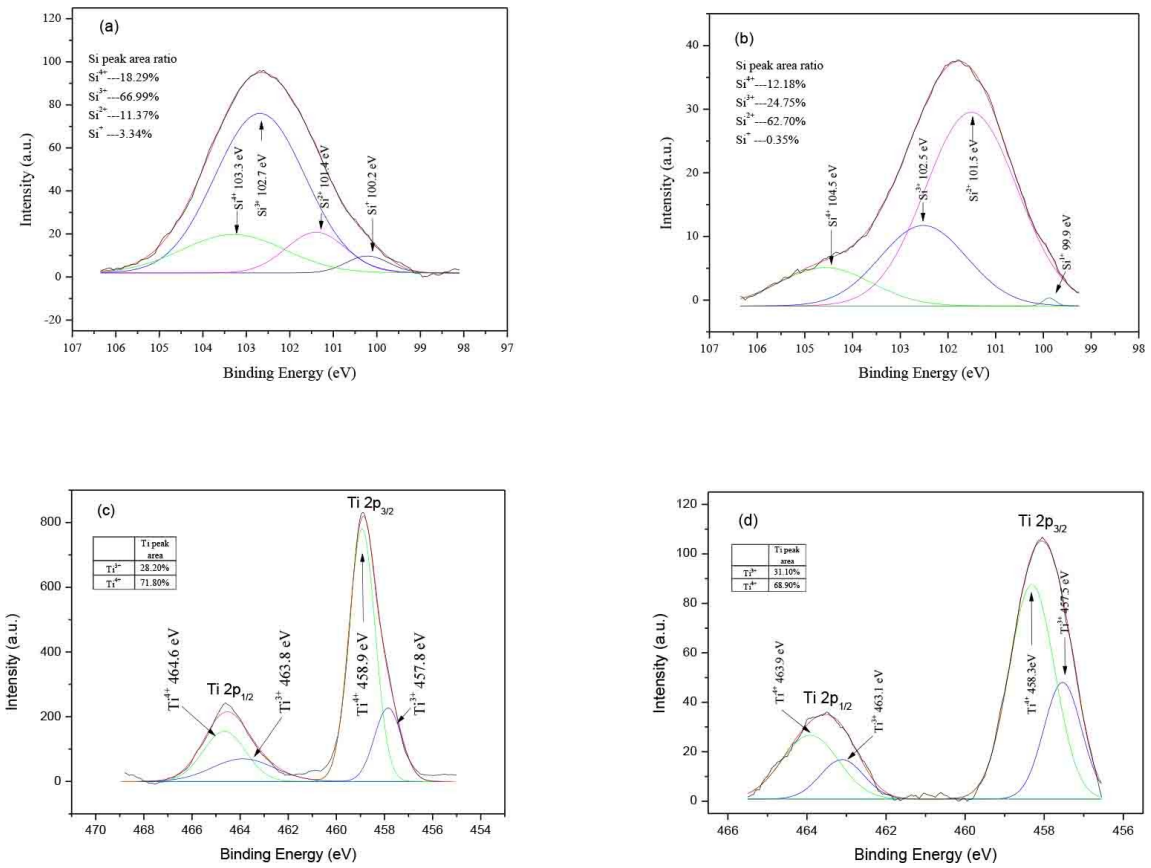

Figure 4. (a) the XPS of Si 2p in fresh $Ti_mSi_nO_l$-CNTs, (b) the XPS of Si 2p in $Ti_mSi_nO_l$-CNTs electrode after charge/discharge 20 cycles (0.10–2.60 V versus metal lithium) and finally charged to 2.6 V in a cell versus metal Lithium, (c) the XPS of Ti $2p_{1/2}$ and $2p_{3/2}$ in fresh $Ti_mSi_nO_l$-CNTs, and (d) the XPS of Ti $2p_{1/2}$ and $2p_{3/2}$ in $Ti_mSi_nO_l$-CNTs electrode after charge/discharge 20 cycles and finally charged to 2.6 V in a cell versus metal Lithium. The spectra are calibrated with C1s at 284.6 eV.

and silicon oxide have high electronic conductivity.[16–18] In the partially reduced material, there are large amount of oxygen vacancies, which also favor the Li ion diffusion.[11] The high electronic conductivity and the high Li ion diffusion rate of the material guarantee it's high rate capable.

The FTIR spectra of fresh $Ti_mSi_nO_l$-CNTs is given in Figure S3A. The peak of Si^{4+}-O-Ti^{4+} bond vibration (that should appear around 930–950 cm^{-1}) is not observed.[39,49,50] In our fresh material, the Si^{n+} cations are mostly in Si^{3+}, Si^{2+}, and Si^{+} valence states, which stand for more than 80% of Si^{n+} ions (see XPS characterizations) and also, the Ti^{n+} cations contain about 28% of Ti^{3+} ions (see our XPS data). Even there are peaks corresponding to Si^{n+}-O-Ti^{m+} bonds, the peaks may not locate in the region of 930–950 cm^{-1}. Most likely, the peaks of Si^{n+}-O-Ti^{m+} bond stretch vibrations overlap with the peaks of Ti^{n+}-O-Ti^{m+} bond vibrations. The easier reducible Ti^{4+} ions that close to Si^{4+}[39] might also be a reason that the vibration peak of Si^{4+}-O-Ti^{4+} at about 950 cm^{-1} is not observed in the FTIR spectra of the fresh $Ti_mSi_nO_l$-CNTs. The prediction is proved by the FTIR spectrum of $Ti_mSi_nO_l$-CNTs that was calcined in air at 500 °C for 5 h. Clearly, over the oxidized $Ti_mSi_nO_l$-CNTs, a peak at 945 cm^{-1} is observed. The peak is assigned to the vibration of Si^{4+}-O-Ti^{4+} bond (Figure S3B).

Figure 5 gives the cyclic voltammograms (CV) of cells for $Ti_mSi_nO_l$-CNTs or $Ti_mSi_nO_l$ cathode versus metal lithium anode. The spectra were recorded on fresh cells. The results show that the curves show significant difference between their first cycle and the following cycles. By comparing the CV curves of their first reduction/oxidation cycle with their following reduction/oxidation cycles, the CV curves show that $Ti_mSi_nO_l$ electrode is more irreversible than $Ti_mSi_nO_l$-CNTs electrode. The irreversible discharge (reduction in the first cycle) could be caused from the SEI formation and the structure change of the materials. After the first cycle, the CV curves of $Ti_mSi_nO_l$-CNTs gives very weak reduction/oxidation peaks at 1675/1851 mV. The weak peaks should be contributed by anatase crystal seeds (see Figure 3c) that are observed in the TEM image [51]. The major discharge occurs below 818 mV. This part of discharge should be contributed by both of TiO_x and SiO_y (see Figure S4). Comparing with that of $Ti_mSi_nO_l$-CNTs, the reduction/oxidation peaks of $Ti_mSi_nO_l$ appear at relatively higher voltage positions (1709/2178 mV). It could also be found that the maximum reduction current (0.32 mA/mg) of $Ti_mSi_nO_l$-CNTs is much bigger than that (0.15 mA/mg) of $Ti_mSi_nO_l$, indicating that $Ti_mSi_nO_l$-CNTs has higher specific capacity and better electronic conductivity than $Ti_mSi_nO_l$. Observing the whole spectra of $Ti_mSi_nO_l$-CNTs and $Ti_mSi_nO_l$, it could also been found that the oxidation/reduction

© 2020 Wiley-VCH Verlag GmbH & Co. KGaA, Weinheim

25666223, 2020, 5, Downloaded from https://chemistry-europe.onlinelibrary.wiley.com/doi/10.1002/batt.201900178 by University of Ulsan, Wiley Online Library on [11/11/2025]. See the Terms and Conditions (https://onlinelibrary.wiley.com/terms-and-conditions) on Wiley Online Library for rules of use; OA articles are governed by the applicable Creative Commons License

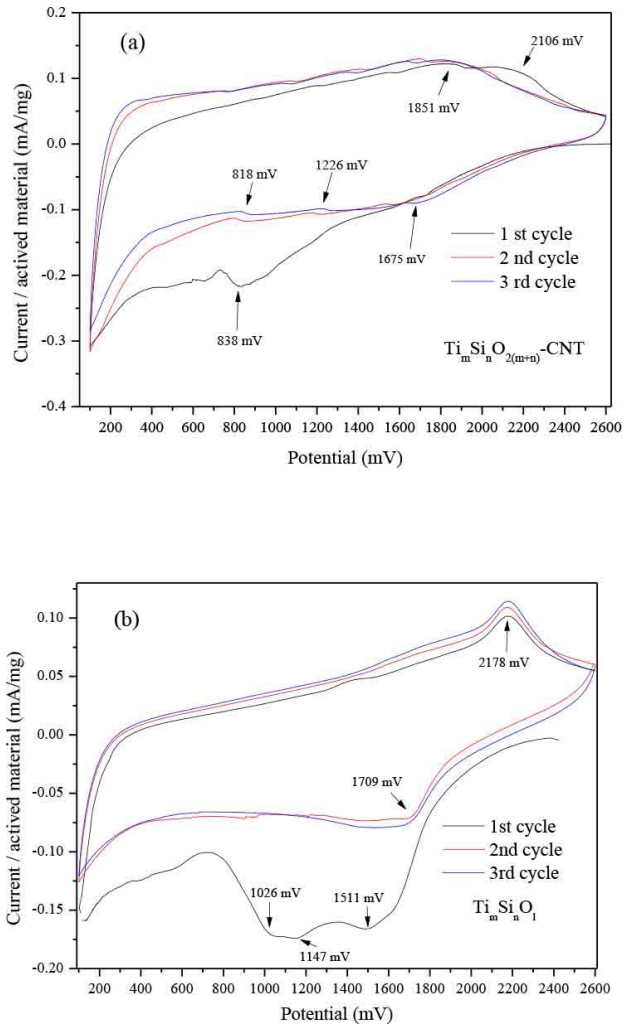

Figure 5. The cyclic voltammograms of (a) cell with $Ti_mSi_nO_l$-CNT versus metal lithium and (b) $Ti_mSi_nO_l$ versus metal lithium were recorded at a potential scan rate of 0.10 mV s^{-1} and a potential window of 0.100–2.600 V.

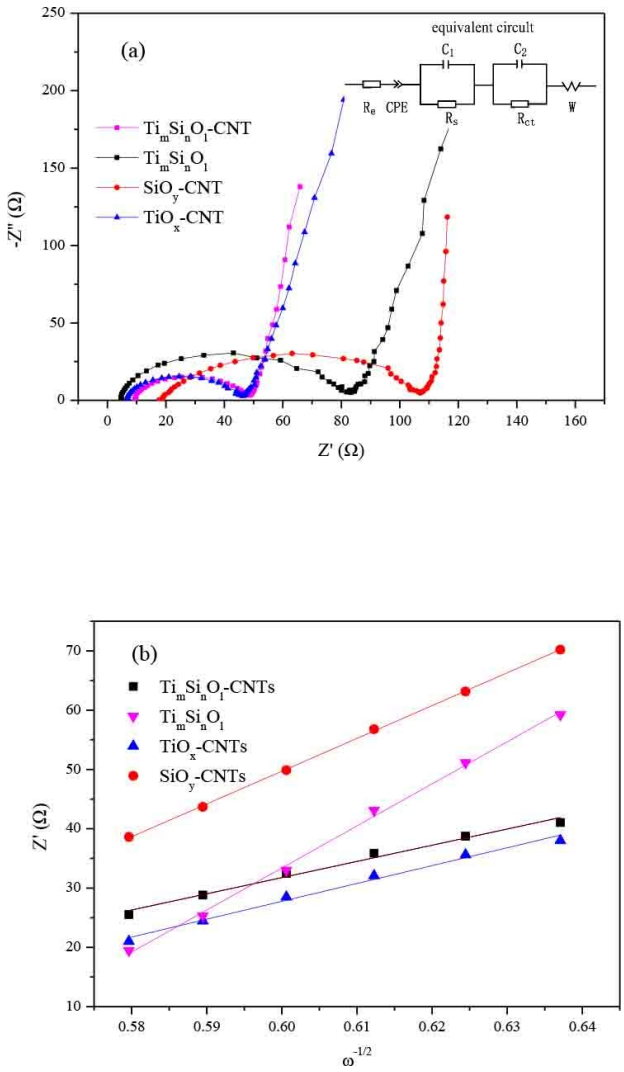

Figure 6. (a) The electrochemical impedance spectra of $Ti_mSi_nO_l$-CNTs, $Ti_mSi_nO_l$, TiO_x-CNTs, and SiO_y-CNTs cells, (b) The $\omega^{-1/2}$ -Z' plots of $Ti_mSi_nO_l$-CNTs, $Ti_mSi_nO_l$, TiO_x-CNTs, and SiO_y-CNTs cells.

peaks at 1851/1675 mV and 2178/1709 mV are not as sharp as that observed for crystal anatase.[17] The potential difference between the oxidation peak and the reduction peak on $Ti_mSi_nO_l$-CNTs is 176 mV, which is much smaller than that (469 mV) of $Ti_mSi_nO_l$. These results indicate that $Ti_mSi_nO_l$-CNTs has much smaller polarization than $Ti_mSi_nO_l$, and therefore, $Ti_mSi_nO_l$-CNTs has much better electric conductivity than $Ti_mSi_nO_l$. The results show that the addition of CNTs enhances the electronic conductivity of $Ti_mSi_nO_l$ and also improves the capacity and reversibility of $Ti_mSi_nO_l$.

Figure 6a shows the electrochemical impedance spectra (EIS) of the materials. The Nyquist plots are fitted by using the equivalent circuit model. All the plots possess a depressed semicircle at high to intermediate frequency and an oblique line at low frequency. The Nyquist plots are fitted by Zsimwin method,[52] and the results are shown in Table S3. R_e represents the electrolyte resistance, R_s is the resistance of the surface film formed on the electrodes. R_{ct} is the charge-transfer resistance. Z_w is the Warburg impedance related to the diffusion of lithium ions into the bulk electrodes.[53–55] The cells with $Ti_mSi_nO_l$-CNTs, $Ti_mSi_nO_l$, TiO_x-CNTs, and SiO_y-CNTs electrodes have very close R_e values. $Ti_mSi_nO_l$-CNTs gives the lowest R_s (6.0 Ω), which is lower than that of $Ti_mSi_nO_l$ (7.8 Ω). This should be attributed to the addition of CNTs, which improves the electronic conductivity of SEI film of $Ti_mSi_nO_l$-CNTs. The interesting thing is that the introducing of SiO_y into TiO_x-CNTs also reduces the R_s value of the material. This could be attributed to the effects that the amorphous SiO_y boundaries isolate the anatase TiO_2 nano domains (as explained in the specific surface area, XRD, SEM, and TEM characterizations). The sub-nano porous SiO_y boundaries might actually hinder the SEI growth. Hence, the SEI around the TiO_2 crystal seeds in $Ti_mSi_nO_l$-CNTs could be thinner than that in TiO_x-CNTs. It is understandable that SiO_y -CNTs gives the highest R_s value, since that silicon oxide is neither a good electronic conductor, nor a good Li ion conductor.

The R_{ct} of $Ti_mSi_nO_l$-CNTs, $Ti_mSi_nO_l$, TiO_x-CNTs, and SiO_y-CNTs are 27.0, 63.6, 33.5, and 94.0 Ω, respectively. The introduction of SiO_y into TiO_x-CNTs improves the charge transfer conductiv-

© 2020 Wiley-VCH Verlag GmbH & Co. KGaA, Weinheim

25666223, 2020, 5, Downloaded from https://chemistry-europe.onlinelibrary.wiley.com/doi/10.1002/batt.201900178 by University of Ulsan, Wiley Online Library on [11/11/2025]. See the Terms and Conditions (https://onlinelibrary.wiley.com/terms-and-conditions) on Wiley Online Library for rules of use; OA articles are governed by the applicable Creative Commons License

ity of TiO_x-CNTs and also, the addition of CNTs into $Ti_mSi_nO_l$ could dramatically improve the charge transfer conductivity of $Ti_mSi_nO_l$. Both of the above improvements make $Ti_mSi_nO_l$-CNTs a better anode material than TiO_x-CNTs.

The lithium ion diffusion coefficient (D_{Li}) of $Ti_mSi_nO_l$-CNTs, $Ti_mSi_nO_l$, TiO_x-CNTs, and SiO_y-CNTs can be calculated from the following Equation (1).

$$D_{Li} = \frac{(RT)^2}{2A^2n^4F^4C_{Li}^2\sigma^2} \quad (1)$$

The A is the area of the electrode. The n is the number of electrons transferred in the electrochemical reaction. The F is the Faraday constant. The C is the concentration of lithium ions in electrode. The σ is the slope of the Z'–$\omega^{-1/2}$ line (Figure 6b). The R is the gas constant. The T is the Kelvin temperature at the time that the experiment is carried out.[39]

The D_{Li} of the materials are calculated and given in Table S3. The $Ti_mSi_nO_l$-CNTs has a D_{Li} of 1.57×10^{-14} cm^2s^{-1}, which is a little bigger than that (1.29×10^{-14} cm^2s^{-1}) of TiO_x-CNTs. The faster Li^+ insertion/extraction kinetics in $Ti_mSi_nO_l$-CNTs than in TiO_x-CNTs might be because of two reasons. One of the reasons is that the TiO_2 crystals in TiO_x-CNTs (obtained at or above 400 °C) are bigger than that in $Ti_mSi_nO_l$-CNTs (obtained at the same temperature as that of TiO_x-CNTs). The other reason could be that the formation of the sub-nano pores in boundary SiO_y phase (around the anatase crystal seeds) offers very rich Li^+ ion diffusion channels. The D_{Li} of SiO_y-CNTs (3.84×10^{-15} cm^2s^{-1}) and $Ti_mSi_nO_l$ (2.32×10^{-15} cm^2s^{-1}) are smaller than that of $Ti_mSi_nO_l$-CNTs and TiO_x-CNTs.

The coulombic efficiencies of the cells from their first discharge/charge cycle to their fourth cycle are 60 (1st), 77 (2nd), 95 (3rd), and 100% (4th), respectively. The results indicate that a stable SEI film is formed within the first 4 cycles of discharge/charge. The results are consistent with that in the CV characterization of $Ti_mSi_nO_l$-CNTs. Over the topic material, there should not be reactions between the anode material and the electrolyte to consume the electrolyte (similar to that happened over the bare Li metal anode).[5,6] In the first discharge, (discharge to 0.10 V versus metal Li), both TiO_2 and SiO_2 could be reduced to lower valence states (SiO_2 starts to be reduced below 0.15 versus Li metal).[6] Possibly, the SiO_y is reduced to irreversible Li_4SiO_4 and reversible $Li_2Si_2O_5$, while TiO_x is reduced to low valence state titanium oxides and Li_2O (irreversible) in the discharge process. Comparing the CV curves (from their first cycle to their third cycle) of cells with $Ti_mSi_nO_l$-CNTs, $Ti_mSi_nO_l$, TiO_x-CNTs, and SiO_y-CNTs cathodes in Figure 5 and Figure S4, it could be found that $Ti_mSi_nO_l$-CNTs gives the highest first cycle reversibility. The first cycle reversibility decrease order is $Ti_mSi_nO_l$-CNTs $>$ $Ti_mSi_nO_l$ $>$ TiO_x-CNTs $>$ SiO_y-CNTs. As discussed in previous sections, the protection of the relatively inert SiO_y boundaries to TiO_2 crystal seeds probably acts an important role to hinder SEI growth in $Ti_mSi_nO_l$-CNTs. Both of TiO_x-CNTs and SiO_y-CNTs consumes a large amount of Li^+ ions to form their SEI in their first cycle of CV scanning.

The electrochemical performances of the $Ti_mSi_nO_l$-CNTs materials calcined at different temperatures are given Figure S5. It is found that the optimum calcination temperature of $Ti_mSi_nO_l$-CNTs is 400 °C. The $Ti_mSi_nO_l$-CNTs prepared at 400 °C gives the highest specific capacity and the highest rate capability. Figure 7a gives the discharge/charge curves of the cells in their 20th cycle (between 0.10 and 2.60 V at 100 mAg^{-1}) with the topic materials as cathodes versus lithium metal anodes. The results show that the specific capacities of the materials increase according to the order: SiO_y-CNTs $<$ TiO_x-CNTs, $Ti_mSi_nO_l$ $<$ $Ti_mSi_nO_l$-CNTs. The SiO_y-CNTs cell gives the lowest capacity. The reason is that the low intrinsic electronic and ionic conductivities of silicon suboxides usually lead to an inferior rate performance and lower reversible capacity because of Li_2O and Li_4SiO_4 formation.[39,56,57]

Generally, Li insertion into the anatase phase is a multistep process, likely including solid–solution formation, a first-order phase transition (two-phase reaction), and interfacial storage. There is usually a plateau at about 1.8 to 2.0 V.[58] However, on the discharge/charge curves of TiO_x-CNTs, $Ti_mSi_nO_l$, and $Ti_mSi_nO_l$-CNTs cells, except the slightly bending of curves at about 2.0 V, there is no apparent plateau observed.[17, 58] The bending of the discharge/charge curves of TiO_x-CNTs, $Ti_mSi_nO_l$, and $Ti_mSi_nO_l$-CNTs cells at about 2.0 V should be caused by the anatase crystal seeds, which are observed in the TEM image. The major parts of the discharge/charge curves of these cells show characters of amorphous phase materials.

Figure 7b shows the rate performances of $Ti_mSi_nO_l$-CNTs, $Ti_mSi_nO_l$, TiO_x-CNTs, and SiO_y-CNTs at different current densities. The $Ti_mSi_nO_l$-CNTs gives the best rate capability. High specific capacities of 302 and 152 $mAhg^{-1}$ are obtained at current densities of 100 and 4000 mAg^{-1}, respectively. The TiO_x-CNTs electrode has a specific capacity close to that of $Ti_mSi_nO_l$-CNTs in the first few cycles, but degrades quickly within the first 20 cycles of discharge/charge. In the following discharge/charge cycles of different current densities, the specific capacities of TiO_x-CNTs electrode ranks the second. The specific capacity of $Ti_mSi_nO_l$ ranks the third at current densities below 2000 mAg^{-1}. Different from $Ti_mSi_nO_l$-CNTs and TiO_x-CNTs, more specific capacity loss is observed on $Ti_mSi_nO_l$ at higher current densities. At current densities higher than 2000 mAg^{-1}, $Ti_mSi_nO_l$ gives very low specific capacity (even lower than that of SiO_y-CNTs). SiO_y-CNTs gives the lowest specific capacities at current densities below 2000 mAg^{-1}. The performances of TiO_x-CNTs and $Ti_mSi_nO_l$-CNTs indicate that the addition of SiO_y into TiO_x-CNTs improves both the rate capability and the cycling stability of TiO_x-CNTs. The performances of $Ti_mSi_nO_l$ and $Ti_mSi_nO_l$-CNTs indicate that the addition of CNTs into $Ti_mSi_nO_l$ also improves both the rate capability and the specific capacity of $Ti_mSi_nO_l$.

Figure 7c gives the cycling life-time test results of the cells with $Ti_mSi_nO_l$-CNTs, $Ti_mSi_nO_l$, TiO_x-CNTs, or SiO_y-CNTs as cathode versus metal lithium anode. Over $Ti_mSi_nO_l$-CNTs, there is capacity degrade in the first 20 cycles. The initial capacity decline of $Ti_mSi_nO_l$-CNTs is possibly due to the formations of cracks, and thus the electrical contact loss of partial active particles and the generation of dead lithium in the $Ti_mSi_nO_l$ matrix. After about 20 cycles of discharge/charge, the electrode reaches a stable state, delivering a high and stable specific capacity of *ca.* 276 $mAhg^{-1}$. The $Ti_mSi_nO_l$-CNTs gives the highest

© 2020 Wiley-VCH Verlag GmbH & Co. KGaA, Weinheim

25666223, 2020, 5, Downloaded from https://chemistry-europe.onlinelibrary.wiley.com/doi/10.1002/batt.201900178 by University of Ulsan, Wiley Online Library on [11/11/2025]. See the Terms and Conditions (https://onlinelibrary.wiley.com/terms-and-conditions) on Wiley Online Library for rules of use; OA articles are governed by the applicable Creative Commons License

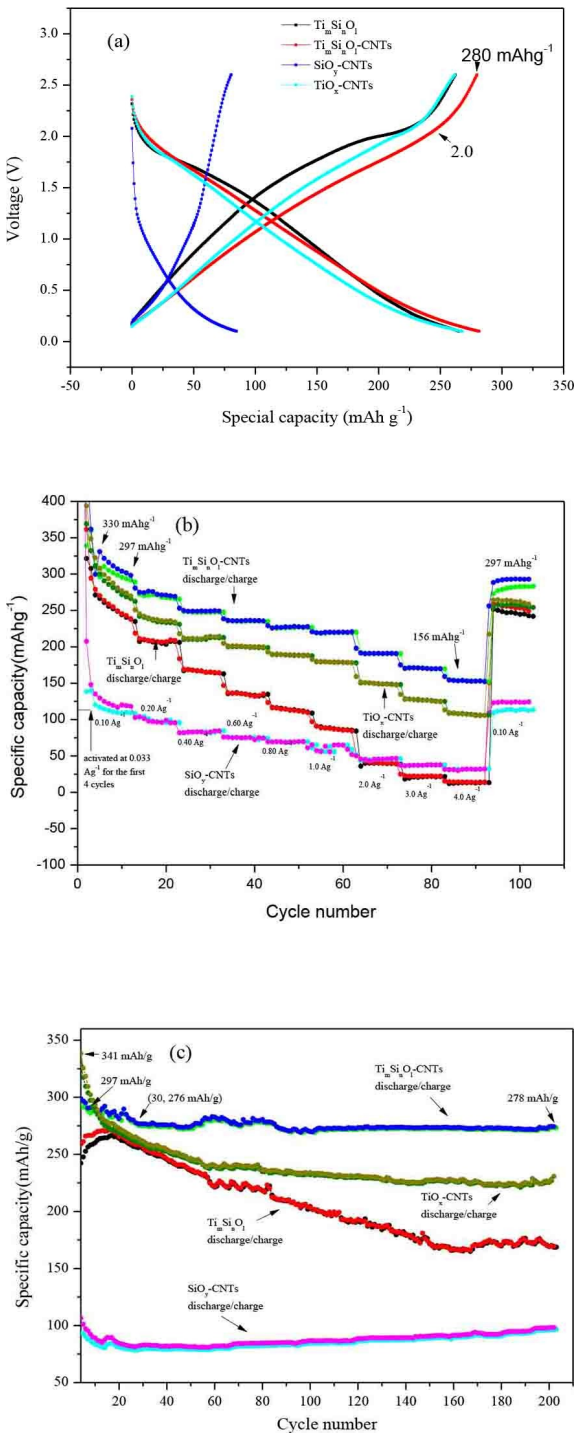

Figure 7. The discharge/charge performances of $Ti_mSi_nO_l$-CNTs, $Ti_mSi_nO_l$, TiO_x-CNTs, and SiO_y-CNTs cells with lithium metal anodes between 0.10 −2.60 V. (a) the discharge/charge curves (electrode loading: $Ti_mSi_nO_{2(m+n)}$ 1.4 mg/cm^2, $Ti_mSi_nO_l$-CNTs 1.4 mg/cm^2, TiO_x-CNTs 1.1 mg/cm^2, SiO_y-CNTs 1.1 mg/cm^2; test conditions: 0.10-2.60 V, 0.10 Ag^{-1}). (b) The discharge/charge performances at 0.10, 0.20, 0.40, 0.60, 0.80, 1.00, 2.00, 3.00, 4.00, and 0.10 Ag^{-1} and between 0.10 and 2.60 V (electrode loading: $Ti_mSi_nO_l$ 1.4 mg/cm^2, $Ti_mSi_nO_l$-CNTs 1.4 mg/cm^2, TiO_x-CNTs 1.2 mg/cm^2, SiO_y-CNTs 1.2 mg/cm^2; test conditions: 0.10-2.60 V, 0.10 A/g). (c) the discharge/charge performances at constant current density 0.10 Ag^{-1} (electrode loading: $Ti_mSi_nO_l$ 1.4 mg/cm^2, $Ti_mSi_nO_l$-CNTs 1.4 mg/cm^2, TiO_x-CNTs 1.1 mg/cm^2, SiO_y-CNTs 1.1 mg/cm^2; test conditions: 0.10-2.60 V, 0.10 A/g). The relative errors of the data from cell to cell is about ±3.3%.

reversable specific capacity (276 mAhg^{-1} at 100 mAg^{-1}) and stability. The TiO_x-CNTs gives higher specific capacity in the first 10 cycles of discharge/charge than $Ti_mSi_nO_l$-CNTs. However, the specific capacity of TiO_x-CNTs degrades very quickly. After 200 cycles of discharge/charge, the specific capacity of TiO_x-CNTs decreases to 225 mAhg^{-1}, which is much lower than that of $Ti_mSi_nO_l$-CNTs (278 mAhg^{-1}). $Ti_mSi_nO_l$ gives lower capacity than $Ti_mSi_nO_l$-CNTs and TiO_x-CNTs, and also, $Ti_mSi_nO_l$ has the worst stability among the 4 materials. SiO_y-CNTs shows higher stability, but lower capacity than the other 3 materials. The addition of SiO_y into TiO_x-CNTs improves the stability, rate capability, and the specific capacity of TiO_x-CNTs. The addition of CNTs into $Ti_mSi_nO_l$ also improves both the stability and the specific capacity of $Ti_mSi_nO_l$.

The excellent electrochemical performances of $Ti_mSi_nO_l$-CNTs could be because of that the specific synthesis method offers a metal organic polymer. The decomposition of the metal organic polymer (at high temperature) yields amorphous carbon and a solid solution $Ti_mSi_nO_l$ with CNTs encapsulated in it. In the following crystallization process of TiO_2, the Ti^{4+} ions migrate together from the nearby positions to form anatase TiO_2 crystal seeds or crystals and leave amorphous SiO_y behind to form boundaries around the TiO_2 crystal seeds or crystals. Since the moving out of Ti^{4+} ions, there must be defects or pores left in the amorphous SiO_y phase. Hence, finally form the typical structure that anatase TiO_2 crystal seeds or crystals are surrounded by the amorphous SiO_y, which has sub-nano pores. The CNTs and the amorphous carbon form an efficient electronic conductive network both inside the particles and between any nearby particles. This electronic conductive network could transfer electrons to nano meter level $Ti_mSi_nO_l$ zones. Hence, the titanium oxides and silicon oxides have enough chances to access electrons and Li^+ ions. Hence, $Ti_mSi_nO_l$-CNTs could accept more lithium ions to have high specific capacity. The CNTs could also act a role of elastic binder to enhance the stability of $Ti_mSi_nO_l$-CNTs particles to tolerate the volume change in charge/discharge process. On one hand, the existing of SiO_y boundaries around the TiO_2 crystal seeds or crystals might hinder the continuous growth of SEI on TiO_2 crystals to stabilize the thickness of SEI, on the other hand, the existing of SiO_y boundaries might render TiO_2 crystals more durable to volume change in charge/discharge process. Hence, the effects of SiO_y boundaries could be the reasons that the introducing of SiO_y into TiO_x-CNTs improves the electrochemical performances of TiO_x-CNTs. The existing of SiO_y boundaries around the TiO_2 crystals also hinders the growth of TiO_2 crystals. Smaller TiO_2 crystal size favours the Li^+ ion diffusion. The sub-nano pores in the SiO_y boundaries also offer very rich Li^+ ion diffusion channels. Both of the small TiO_2 crystal size and the sub-nano pores in SiO_y boundaries render $Ti_mSi_nO_l$-CNTs have high D_{Li+} and guarantee the high rate capability of the material.

© 2020 Wiley-VCH Verlag GmbH & Co. KGaA, Weinheim

25666223, 2020, 5, Downloaded from https://chemistry-europe.onlinelibrary.wiley.com/doi/10.1002/batt.201900178 by University of Ulsan, Wiley Online Library on [11/11/2025]. See the Terms and Conditions (https://onlinelibrary.wiley.com/terms-and-conditions) on Wiley Online Library for rules of use; OA articles are governed by the applicable Creative Commons License

3. Conclusions

An anode material, $Ti_mSi_nO_l$-CNTs, was prepared by a specific synthesis method for its application in lithium-ion batteries (LIBs). The $Ti_mSi_nO_l$-CNTs has a typical structure in which: (1) the CNTs are encapsulated in $Ti_mSi_nO_l$, (2) the amorphous carbon is formed from the decomposition of ethylene glycol, (3) the anatase TiO_2 crystal seeds or crystals are encapsulated in SiO_y boundaries, and, (4) the SiO_y boundaries are porous amorphous silicon oxide (or amorphous silicon oxide with large number of defects). The excellent electric conductivity of CNTs and the amorphous carbon gives more chances for TiO_x and SiO_y to access electrons and accommodate more Li+ ions to raise the specific capacity and reduces the polarization of $Ti_mSi_nO_l$. The CNTs might also act a role of elastic binder of the $Ti_mSi_nO_l$-CNTs particles to enhance the stability of $Ti_mSi_nO_l$-CNTs. The existing of SiO_y boundaries around the TiO_2 crystal seeds or crystals makes the anatase TiO_2 more stable in charge/discharge process. The existing of SiO_y boundaries around TiO_2 crystal seeds or crystals hinders the growth of TiO_2 crystals to keep the TiO_2 crystals in nanometer level, which favours the Li^+ ion diffusion. The sub-nano pores in the SiO_y boundaries also offer very rich Li^+ ion diffusion channels. Both of the small TiO_2 crystal size and the sub-nano pores in SiO_y boundaries render $Ti_mSi_nO_l$-CNTs have high D_{Li+} and guarantee the high rate capability of the material. Finally, this investigation work gives a simple method to synthesize a high performance anode material $Ti_mSi_nO_l$-CNTs, which has high rate capability, high stability, and high specific capacity. It could be easily scale up to industry scale. The material works at a reduction potential of 0.10 V higher than metal lithium. The relatively higher (than metal lithium) reduction potential of the material could effectively avoids lithium plating on the anode in the charge process of the full cells.

Experimental Section

The $Ti_mSi_nO_l$-CNTs composites were synthesized by the following method. Carbon nanotubes (0.7500 g), anhydrous ethylene glycol (42.0 g), tetrapropyl orthosilicate (3.47 g), titanium (IV) isopropoxide (10.69 g), and *N*,*N*-dimethylhexadecylamine (0.0100 g, catalyst) are added into a Teflon-lined stainless steel autoclave under stirring in an argon filled glove box. The autoclave is sealed and fixed on a rotation axis (driven by an electronic motor) in an oven. The rate of the axis rotation is set to 10 r/min and the temperature of the oven is 140 °C. The reaction is let to complete at 140 °C for 6 h. After completing the reaction, the mixture is filtrated and washed by ethanol (50 ml) to obtain the titanium-silicon-ethylene glycol polymer encapsulated CNTs (supposed to be $Ti_mSi_n(OCH_2CH_2O)_{2(m+n)}$-CNTs). The solid product is calcined at desired temperatures (between 400 and 700 °C) in nitrogen for 5 h to obtain $Ti_mSi_nO_l$-CNTs composites. Materials TiO_x-CNTs, SiO_y-CNTs, and $Ti_mSi_nO_l$ were also synthesized by the same method at different temperatures, without adding tetrapropyl orthosilicate, titanium (IV) isopropoxide, and CNTs, respectively.

The TGA measurement was conducted from 25 °C to 800 °C with a heating rate of 20 °C/min in high purity N_2. The element analysis was carried out on a XRF-1800 (Shimadzu) instrument. The X-ray diffraction (XRD) patterns were recorded with a Bruker D8 powder X-ray diffractometer (Germany) using Cu K_α radiation (40 kV, 40 mA). The spectra were recorded from 10° to 80°. The surface morphology and microstructure of the samples were characterized by SEM (Nova Nano, SEM 230).

Transmission electron microscopy (TEM) experiments were conducted on a TEM (Titan G2 60–300 FEI) operated at 300 kV. Nitrogen sorption isotherms were measured at 77 K with a NOVA2200e (Quantachrome Instruments) analyzer. All of the samples were degassed under vacuum at 200 °C for at least 2 h prior to the measurements. The Brunauer-Emmett-Teller (BET) method was utilized to calculate the specific surface area. The FTIR spectra were recorded on a Nicolet iS50 spectroscopy. The X-ray photoelectron spectroscopy (XPS) was recorded on an AXIS ULTRA DLD XPS System with MONO Al source (Shimadzu Corp.). Photoelectron spectrometer was recorded by using monochromatic Al K_R radiation. All of the binding energies were referenced to the C1s peak at 284.6 eV of the surface adventitious carbon.

The as-prepared anode material, conductive carbon black, carbon nanotubes (dispersed in N-methyl-2-pyrrolidone), polyvinylidene fluoride (PVDF) binder (dissolved in N-methyl-2-pyrrolidone) were mixed according to the mass ratio of 85:10:1.5:3.5 to prepare a paste. The paste was coated on a copper foil (the thickness of the anode coating layer is 90 μm) with an applicator (frame-type), and then dried in a vacuum oven at 120 °C for 2 h to obtain the anode plate. The dried anode plate was cut into cycles with a diameter of 14 mm. The anode cycles were farther dried in a tubular furnace (filled with argon) at 140 °C for 5 hours, and then transferred into an argon filled glove box (Mikrouna) in argon atmospheres. The anode cycles together with the separator (PP), the lithium metal cycles (as the counter electrode), and the electrolyte solution (1.0 M of $LiPF_6$ in EC, PC, DMC, and EMC, the volume ratio of EC:PC:DMC:EMC is 1:1:1:1) were used to assemble coin-type cells. The mass loadings of materials in each cells are: 2.0 mg ($Ti_mSi_nO_{2(m+n)}$), 2.0 mg ($Ti_mSi_nO_l$-CNTs), 1.5 mg (TiO_x-CNTs), 1.5 mg (SiO_y-CNTs). In each cell, 60 μl of electrolyte solution is used.

The discharge/charge tests of the cells were carried out on a NEWARE CT-3008-5 V-10 mA system. The voltage window is set as 0.10 ~ 2.60 V (vs. Li / Li^+) to control the reduction level of SiO_y to avoid over reduction of SiO_y (over reduction of SiO_y could lead to formation of too much of Li_2O and Li_4SiO_4, which are harmful to electrode.[5,6, 39] The cycling voltammetry curves were recorded on an electrochemical workstation (CHI 660E, CHENHUA) at a scan rate of 0.1 mV s^{-1} within 0.10 V and 2.60 V (vs. Li/Li^+). The electrochemical impedance spectra (EIS) of the cells were recorded on an electrochemical workstation (CHI 660E, CHENHUA). EIS were collected from 100 kHz to 0.010 Hz with a perturbation voltage of 5.0 mV. All tests were carried out at room temperature.

Acknowledgements

Thanks for the financial support from the Zhejiang Folta Technologies Inc. and the China Hunan Provincial Science & Technology Department (2017NK1013) is gratefully acknowledged.

Keywords: silicon oxide anode · titanium oxide anode · lithium ion battery

[1] F. Orsini, A. D. Pasquier, B. Beaudoin, J. M. Tarascon, M. Trentin, N. Langenhuizen, E. D. Beer, P. Notten, *J. Power Sources* **1998**, *76*, 19.

© 2020 Wiley-VCH Verlag GmbH & Co. KGaA, Weinheim

25666223, 2020, 5, Downloaded from https://chemistry-europe.onlinelibrary.wiley.com/doi/10.1002/batt.201900178 by University of Ulsan, Wiley Online Library on [11/11/2025]. See the Terms and Conditions (https://onlinelibrary.wiley.com/terms-and-conditions) on Wiley Online Library for rules of use; OA articles are governed by the applicable Creative Commons License

[2] A. Gurung, K. Chen, R. Khan, S. S. Abdulkarim, G. Varnekar, R. Pathak, R. Naderi, Q. Q. Qiao, *Adv. Energy Mater.* **2017**, *7*, 1602105.
[3] J. Haetge, P. Hartmann, K. Brezesinski, J. Janek, T. Brezesinski, *Chem. Mater.* **2011**, *23*, 4384.
[4] L. F. Shen, C. Z. Yuan, H. J. Luo, X. G. Zhang, S. D. Yang, X. J. Lu, *Nanoscale* **2011**, *3*, 572.
[5] R. Pathak, K. Chen, A. Gurung, K. M. Reza, B. Bahrami, F. Wu, A. Chaudhary, N. Ghimire, B. Zhou, W. H. Zhang, Y. Zhou, Q. Q. Qiao, *Adv. Energy Mater.* **2019**, *36*, 1901486.
[6] K. Chen, R. Pathak, A. Gurung, E. A. Adhamash, B. Bahrami, Q. Q. He, H. Qiao, A. L. Smirnova, J. J. Wu, Q. Q. Qiao, Y. Zhou, *Energy Storage Mater.* **2019**, *18*, 389.
[7] M. McGraw, P. Kolla, B. Yao, R. Cook, Q. Quiao, J. Wu, A. Smirnova, *Polymer* **2016**, *99*, 488.
[8] A. Gurung, R. Naderi, B. Vaagensmith, G. Varnekar, Z. P. Zhou, H. Elbohy, Q. Q. Qiao, *Electrochim. Acta* **2016**, *211*, 720.
[9] S. Liu, W. W. Lei, Y. Liu, Q. Q. Qiao, W. H. Zhang, *ACS Appl. Mater. Interfaces* **2018**, *10*, 37445.
[10] S. J. P. Varapragasam, C. Balasanthiran, A. Gurung, Q. Q. Qiao, R. M. Rioux, J. D. Hoefelmeyer, *J. Phys. Chem. C* **2017**, *121*, 11089.
[11] R. Pathak, A. Gurung, H. Elbohy, K. Chen, K. M. Reza, B. Bahrami, S. Mabrouk, R. Ghimire, M. Hummel, Z. R. Gu, X. M. Wang, Y. C. Wu, Y. Zhou, Q. Q. Qiao, *Nanoscale* **2018**, *10*, 15956.
[12] C. K. Chan, H. Peng, G. Liu, K. McIlwrath, X. F. Zhang, R. A. Huggins, Y. Cui, *Nat. Nanotechnol.* **2008**, *3*, 31.
[13] W. C. Mackrodt, *J. Solid State Chem.* **1999**, *142*, 428.
[14] S. J. Bao, Q. L. Bao, C. M. Li, Z. L. Dong, *Electrochem. Commun.* **2007**, *9*, 1233.
[15] S. Takai, M. Kamata, S. Fujine, K. Yoneda, K. Kanda, T. Esaka, *Solid State Ionics* **1999**, *123*, 165.
[16] P. Roy, S. K. Srivastava, *J. Mater. Chem. A* **2015**, 3, 2454.
[17] C. H. Sun, X. H. Yang, J. S. Chen, Z. Li, X. W. Lou, C. Z. Li, S. C. Smith, G. Q. Lu, H. G. Yang, *Chem. Commun.* **2010**, *46*, 6129.
[18] L. H. Nguyen, V. Aravindan, S. A. Kulkarni, Y. Fang, R. R. Prabhakar, S. K. Batabyal, S. Madhavi, *ChemElectroChem* **2014**, *1*, 539.
[19] C. L. Olson, J. Nelson, M. S. Islam, *J. Phys. Chem. B* **2006**, *110*, 9995.
[20] A. Stashans, S. Lunell, R. Bergström, A. Hagfeldt, S. E. Lindquist, *Phys. Rev. B* **1996**, *53*, 159.
[21] M. V. Koudriachova, N. M. Harrison, S. W. Leeuw, *Phys. Rev. B* **2002**, *65*, 235423.
[22] T. Ohzuku, Z. Takehara, S. Yoshizawa, *Electrochim. Acta* **1979**, *24*, 219.
[23] C. J. Howard, T. M. Sabine, F. Dickson, *Acta Crystallogr. Sect. B* **1991**, *47*, 462.
[24] M. Wagemaker, A. A. van Well, G. J. Kearley, F. M. Mulder, *Solid State Ionics* **2004**, *175*, 191.
[25] S. Lunell, A. Stashans, L. Ojamäe, H. Lindström, A. Hagfeldt, *J. Am. Chem. Soc.* **1997**, *119*, 7374.
[26] F. Tielens, M. Calatayud, A. Beltran, C. Minot, J. Andres, *J. Electroanal. Chem.* **2005**, *581*, 216.
[27] L. Kavan, J. Rathouský, M. Grätzel, V. Shklover, A. Zukal, *J. Phys. Chem. B* **2000**, *104*, 12012.
[28] L. Kavan, K. Kratochvilová, M. Grätzel, *J. Electroanal. Chem.* **1995**, *394*, 93.
[29] X. P. Gao, Y. Lan, H. Y. Zhu, J. W. Liu, Y. P. Ge, F. Wu, D. Y. Song, *Electrochem. Solid-State Lett.* **2005**, *8*, A26.
[30] J. R. Li, Z. L. Tang, Z. T. Zhang, *Electrochem. Solid-State Lett.* **2005**, *8*, A316.
[31] J. Xu, C. Jia, B. Cao, W. F. Zhang, *Electrochim. Acta* **2007**, *52*, 8044.
[32] J. Kim, J. Cho, *J. Electrochem. Soc.* **2007**, *154*, A542.
[33] B. Chen, E. Liu, T. T. Cao, F. He, C. S. Shi, C. N. He, L. Y. Ma, Q. Y. Li, J. J. Li, N. Q. Zhao, *Nano Energy* **2017**, *33*, 247.
[34] X. Y. Wang, L. Fan, D. C. Gong, J. Zhu, Q. F. Zhang, B. G. Lu, *Adv. Funct. Mater.* **2016**, *26*, 1104.
[35] J. H. Lee, M. H. Hon, Y. W. Chung, I. C. Leu, *Appl. Phys. A* **2011**, *102*, 550.
[36] M. A. Kanjwal, N. A. M. Barakat, F. A. Sheikh, M. S. Khil, H. Y. Kim, *Int. J. Appl. Ceram. Technol.* **2010**, *7*, E54.
[37] G. D. Du, Z. P. Guo, P. Zhang, Y. Li, M. B. Chen, D. Wexler, H. K. Liu, *J. Mater. Chem.* **2010**, *20*, 5689.
[38] X. X. Wang, M. Xi, X. H. Wang, H. Fong, Z. T. Zhu, *Electrochim. Acta* **2016**, *190*, 811.
[39] Z. L. Li, H. L. Zhao, P. P. Lv, Z. J. Zhang, Y. Zhang, Z. H. Du, Y. Q. Teng, L. Zhao, Z. M. Zhu, *Adv. Funct. Mater.* **2018**, *28*, 1605711.
[40] F. F. Cao, Y. G. Guo, S. F. Zheng, X. L. Wu, L. Y. Jiang, R. R. Bi, L. J. Wan, J. Maier, *Chem. Mater.* **2010**, *22*, 1908.
[41] J. Xu, Y. Wang, Z. Li, W. F. Zhang, *J. Power Sources* **2008**, *175*, 903.
[42] S. C. Pillai, P. Periyat, R. George, D. E. McCormack, M. K. Seery, H. Hayden, J. Colreavy, D. Corr, S. J. Hinder, *J. Phys. Chem. C* **2007**, *111*, 1605.
[43] F. Mei, C. Liu, L. Zhang, F. Ren, L. Zhou, W. Zhao, Y. Fang, *J. Cryst. Growth* **2006**, *292*, 87.
[44] G. Zhang, H. B. Wu, T. Song, U. Paik, X. W. Lou, *Angew. Chem. Int. Ed.* **2014**, *53*, 12590.
[45] K. Xu, L. Ben, H. Li, X. Huang, *Nano Res.* **2015**, *8*, 2654.
[46] L. Shi, W. Wang, A. Wang, K. Yuan, Z. Jin, Y. Yang, *J. Power Sources* **2016**, *318*, 184.
[47] Y. Choi, T. Umebayashi, M. Yoshikawa, *J. Mater. Sci.* **2004**, *39*, 1837.
[48] R. Gouttebaron, D. Cornelissen, R. Snyders, J. P. Dauchot, M. Wautelet, M. Hecq, *Surf. Interface Anal.* **2000**, *30*, 527.
[49] S. Vives, C. Meunier, *Ceram. Int.* **2008**, *34*, 37.
[50] J. P. Rainho, J. Rocha, L. D. Carlos, R. M. Almeida, *J. Mater. Res.* **2001**, *16*, 2369.
[51] S. J. Ding, J. S. Chen, X. W. Lou, *Adv. Funct. Mater.* **2011**, *21*, 4120.
[52] N. Cao, Z. Song, Q. Liang, X. Gao, X. Qin, *Electrochim. Acta* **2017**, *235*, 200.
[53] D. Vladikova, Z. Stoynov, *J. Electroanal. Chem.* **2004**, *572*, 377.
[54] W. Yue, S. Tao, J. Fu, Z. Gao, Y. Ren, *Carbon* **2013**, *65*, 97.
[55] A. Gurung, J. Pokharel, A. Baniya, R. Pathak, K. Chen, B. Sagar Lamsal, N. Ghimire, W. H. Zhang, Y. Zhou, Q. Q. Qiao, *Sustain. Energ. Fuels* **2019**, *12*, 3279.
[56] C. Guo, D. Wang, T. Liu, J. Zhu, X. Lang, *J. Mater. Chem. A* **2014**, *2*, 3521.
[57] Z. Yuan, N. Zhao, C. Shi, E. Liu, C. He, F. He, *Chem. Phys. Lett.* **2016**, *651*, 19.
[58] P. S. Kumar, V. Aravindan, J. Sundaramurthy, V. Thavasi, S. G. Mhaisalkar, S. Ramakrishna, S. Madhavi, *RSC Adv.* **2012**, *2*, 7983.

Manuscript received: November 14, 2019
Revised manuscript received: January 16, 2020
Version of record online: February 3, 2020

© 2020 Wiley-VCH Verlag GmbH & Co. KGaA, Weinheim

25666223, 2020, 5, Downloaded from https://chemistry-europe.onlinelibrary.wiley.com/doi/10.1002/batt.201900178 by University of Ulsan, Wiley Online Library on [11/11/2025]. See the Terms and Conditions (https://onlinelibrary.wiley.com/terms-and-conditions) on Wiley Online Library for rules of use; OA articles are governed by the applicable Creative Commons License